Far-Field Stress Predictions for Utah FORGE Well 16B(78)-32 Under Thermal and Pore Pressure Variations

Report documenting completion of Milestones 4.2.2 and 4.3.1 of Utah FORGE Project 2-2439v2: A Multi-Component Approach to Characterizing In-Situ Stress at the U.S. DOE FORGE EGS Site: Laboratory, Modeling and Field Measurement

Guanyi Lu[a], Ayyaz Mustafa[a], and Andrew P. Bunger[a,b,*]

[a] Department of Civil and Environmental Engineering, University of Pittsburgh, Pittsburgh, PA, USA

[b] Department of Chemical and Petroleum Engineering, University of Pittsburgh, Pittsburgh, PA, USA

*Corresponding author: bunger@pitt.edu

Table of Contents

List of Figures

List of Tables

1. Abstract

We report (1) the far-field stress predictions at five locations along the inclined section of well 16B(78)-32 using the physics-based thermo-poro-mechanical model, fulfilling Milestone 4.2.2; and (2) stress profiles along the entire inclined section of the well under various drilling and pre-cooling scenarios, fulfilling Milestone 4.3.1.

2. Task and milestone description

The main objective of **Task 4.2** is connecting the near-wellbore data measured at Utah FORGE Enhanced Geothermal System (EGS) site to the far-field (away from the wellbore) stresses under various thermal conditions using the physics-based model developed in Task 4.1. **Milestone 4.2.2** entails predicting the far-field stresses based on near-wellbore estimates for Well 16B(78)-32.

The main objective of **Task 4.3** is to predict near well and far-field stress values associated with thermal and pore pressure variation across varying in-situ conditions to bound uncertainties in stress estimation arising from thermo-poro-mechanical effects. **Milestone 4.3.1** is achieved by plotting profiles of maximum, intermediate, and minimum stresses from the wellbore under baseline conditions and with thermal and pore pressure perturbations near well 16B(78)-32.

This report documents the completion of **Milestone 4.2.2** and **4.3.1** technical accomplishments as per the Statement of Project Objectives (SOPO) for the project.

3. Methodology

3.1. Overview

The methodology is divided into three main steps: (1) conducting core-based laboratory triaxial ultrasonic velocity (TUV) experiments, (2) developing and applying velocity-to-stress machine learning (ML) models to estimate near-field principal stresses, and (3) utilizing physics-based finite element model to characterize far-field stresses under significant thermo-poro-mechanical effects. The overall workflow is summarized in Figure 1.

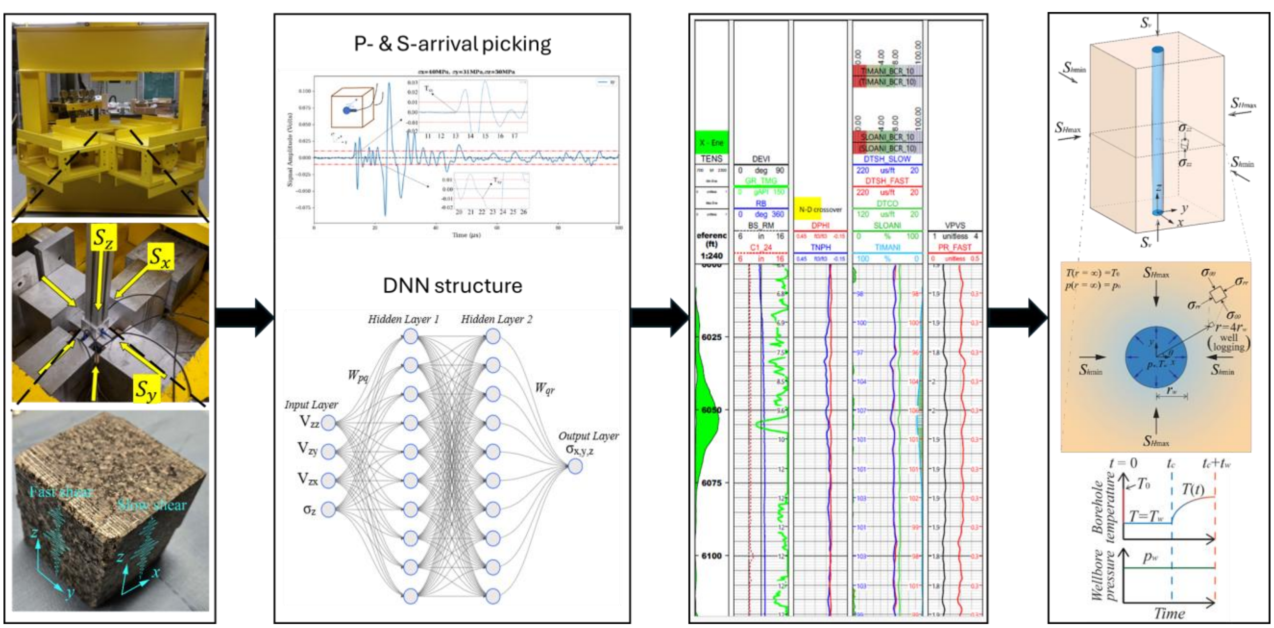

Figure 1: Workflow of the multi-component approach for characterizing in-situ stresses.

Using the data of laboratory TUV experiments, ML models have been developed to establish the velocity-to-stress relationship of three waves generated in lab on FORGE rocks in Task 2. For well 16B(78)-32, core samples were acquired from five different locations from the deviated well section. The core samples represent different rock formations including Gneiss, Granite, Granodiorite, and Quartz gneiss. The measured depths and true vertical depth of these locations are provided in Table 1. Subsequently, the compressional wave along well axis, and the fast and slow (presumably mutually orthogonal) shear waves in the plane transverse to the wellbore are correlated to the three normal stresses acting in the directions corresponding to the wave propagation inside the rock specimens. The resulting predictive model then takes the sonic logging data collected from both wells as the input and estimates all three near-field stresses (Mustafa et al., 2024, 2025). The predicted near-field stresses, namely S_1, S_2, and S_3, are provided in Table 1.

Table 1: Depths, ML predicted near-field stresses, and photos of cubic samples used for TUV experiments.

Rock Type	Core ID	Measured Depth (ft)	True Vertical Depth (ft)	S_1 (MPa)	S_2 (MPa)	S_3 (MPa)	Cubic samples
Gneiss	i	10,438	8,170	61.72	49.52	43.38	
Granite	ii	10,253	8,090	60.51	48.94	44.51	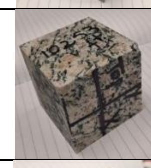
Granodiorite	iii	10,264	8,095	60.84	49.21	44.31	
Quartz Gneiss	iv	9,839	7,925	60.32	49.58	42.32	
Quartz Gneiss	v	9842.3	7,925	60.64	49.64	43.40	

A schematic of well 16B(78)-32, a doublet to the previously drilled injection well 16A(78)-32, is given in Figure 2a. Well 16B(78)-32 was drilled at an azimuth of N105°E (relative to true North), beginning with a vertical section at shallow depths, and followed by a deviated section with an inclination of approximately 65° from the vertical. It is worth noting that although the anticipated minimum horizontal stress, $S_{h\min}$, is trending at N115°E (Xing et al., 2022), which has a 10° offset from the well azimuth. In this analysis, we consider the 10° misalignment would cause negligible difference in overall stress values and therefore impose that the *xz*-plane is parallel to the minimum in-situ stress direction. In contrast, the near-wellbore thermo-poro-mechanical effect in in-situ stress estimation for EGS wells can be significant (Lu et al., 2024a). Since three near-field principal stresses predicted by ML model (Table 1) are based on the sonic logging measurements collected near the well assuming they are collected in an intact rock formation without any near-field stress disturbance. Notably, these near-field stresses can differ from those in the far-field due to borehole stress concentration, pore pressure, and thermo-elastic stress disturbance during drilling and pre-cooling activities (Lu et al., 2024a). Thus, we will invert the problem by imposing these values as the near-field thermo-poro-elastic stresses and compute their corresponding far-field stresses. It is sensible to impose a radial distance ($r = 4r_w$ in this work) from the wellbore center as the representative location of these stresses (Figure 2b). Subsequently, the actual orientations of the three stresses along this perimeter need to be determined by finding the location along which the largest stress-induced wave speed anisotropy occurs. The stress components at the specific location are translated to the corresponding far-field stresses using a numerical model based on Finite Element Method (FEM), combined with semi-analytical solutions, to account for the thermo-poro-elastic stress alteration under specific in-situ conditions (drilling induced stress concentration, poro-elastic stresses, and thermal stresses due to pre-cooling operations) of an EGS well (Lu et al., 2024b, 2025).

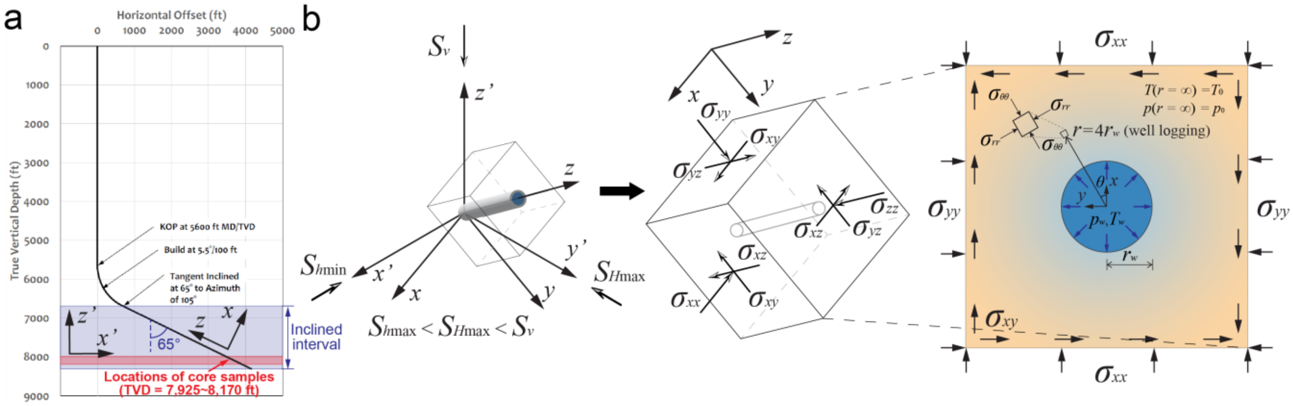

Figure 2: (a) Well trajectory plotted on the vertical plane with the location of core samples collected from well 16B(78)-32. (b) Schematic sketch of an inclined well interval and global/local coordinate systems (right), far-field stresses in the local coordinate system (middle), and planar view of pre-cooling circulation carried out along the well interval (right).

3.2. Predicting far-field stresses in two representative scenarios

To demonstrate this process, two specific scenarios related to drilling and pre-cooling in an EGS well are considered in this study: (1) 10-hour simultaneous pre-cooling circulation and pore pressure diffusion (t_c=10 hours), and (2) followed by 4 hours of warmup (t_w=4 hours). Using the cylindrical coordinate system, the constant temperature, T_w, is imposed at the borehole wall during pre-cooling, while the reservoir has a uniform initial temperature, T_0, and remains constant in far-field (on *xy*-plane) throughout the process. Since temperature (and pressure) changes with depth, we will denote the gradient of temperature difference with depth as $\mathrm{d}\Delta T/\mathrm{d}z' = \mathrm{d}\Delta T_w/\mathrm{d}z' - \mathrm{d}\Delta T_0/\mathrm{d}z'$. Once pre-cooling stops (at $t = t_c$), the temperature boundary condition is removed, and the temperature field during both pre-cooling and the following warmup (at an arbitrary time $t = t_c + t_w$) stages can be solved by the finite element model (see an illustration of the temperature evolution on the borehole wall in Figure 3). In addition, the reservoir is assigned a zero virgin pore pressure, $p_0 = 0$, based on field evidence indicating that the rock is dry in the far-field. Due to the excavation of the well, a constant mud pressure, p_w, is uniformly distributed along the borehole wall. This wellbore pressure increases linearly with depth, following a constant pressure gradient denoted as $\mathrm{d}\Delta p_w/\mathrm{d}z'$. Consequently, the drilling/pre-cooling disturbed stress field is determined by (1) three far-field stresses, (2) mud pressure and pore pressure, and (3) thermal conditions during pre-cooling/warmup. The thermal stresses are obtained by a finite element model using Abaqus, and the remaining poro-elastic stresses are computed using existing analytical and semi-analytical solutions (Cheng, 2016).

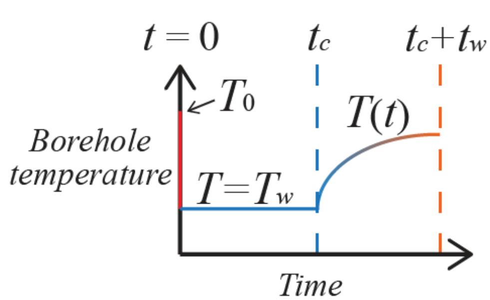

Figure 3: Temperature evolution on borehole wall in the finite element model.

3.3. Determining the location with largest stress-induced wave speed anisotropy

Our numerical model is characterized by constant wellbore pressure and temperature along an interval of the well with radius, r_w. The wellbore is surrounded by a formation subjected to the minimum, intermediate, and maximum far-field principal compressive stresses ($S_{h\min} < S_{H\max} < S_v$). To account for any arbitrary inclination of the wellbore, we begin our stress analysis on the *xy*-plane transverse to the well axis in Figure 2b, and then transform all stresses to the global *x'y'z'* coordinate system for obtaining the far-field stresses aligned with the vertical and two horizontal principal stresses ($S_{h\min}$, $S_{H\max}$, and S_v).

First, a cylindrical coordinate system defined by radius r, angle with respect to the minimum horizontal stress direction, θ, and axial depth z is adopted (Figure 2b). Then, we calculate the three principal stress components predicted by the ML models: radial stress (σ_{rr}), tangential stress ($\sigma_{\theta\theta}$), and the axial stress (σ_{zz}). Recall that, we impose that the sonic logging measurements are taken at a location of $r = 4r_w$, a distance deemed appropriate based on the configuration of the ThruBit (through-the-bit) logging device utilized in well 16B(78)-32. Thanks to its linearity, the problem was decomposed into three distinct components for analysis:

I. **Near-wellbore stress concentration**: Redistributed elastic stresses around a circular wellbore under bi-axial far-field stresses.
II. **Poro-elastic stresses**: Induced by excavation under constant mud pressure acting normal to borehole wall and pore pressure diffusion near the well.
III. **Thermally induced stresses**: Generated by heat conduction during pre-cooling and warm-up.

Linear superposition is used to compute the total thermo-poro-elastic stresses (ML predicted stresses), written as

$$\sigma^{\mathrm{ML}} = \sigma^{\mathrm{I}} + \sigma^{\mathrm{II}} + \sigma^{\mathrm{III}} \tag{1}$$

with tension defined as positive for all stress components σ (ML predicted compressive stresses $S^{\mathrm{ML}} = -\sigma^{\mathrm{ML}}$). Both drilling induced stress concentration (σ^{I}) and the poro-elastic stresses (σ^{II}) due to constant pressure along borehole wall and pressure diffusion into the adjacent rock can be solved using semi-analytical solutions, and a finite element model was developed in Abaqus to compute the radial heat conduction and its induced thermal stresses, σ^{III}. It is worth noting that both σ^{II} and σ^{III} can be solved semi-analytically (Cheng, 2016) and numerically (using the finite element model) for relevant scenarios for EGS (details of the calculations are provided in Lu et al., (2024c, 2025)), while the far-field stresses that cause near-field stress concentration σ^{I} needs to be solved based on near-field ML predictions.

Finding the far-field stresses involve both decoupling the thermo-poro-mechanical effects from the ML predicted total stresses, and accounting for well inclination in determining the spatial locations of the ML-predicted stresses. For the former analysis, semi-analytical solutions and numerical results from the physics-based finite element model are used. As of the well orientation (Figure 2a), the vertical segment of the well extends from the surface to a depth of approximately 5,600 ft (the kick-off point). This is followed by the deviated (build) segment where the well inclination gradually increases. Once the inclination reaches 65°, the well enters a stable, near-horizontal trajectory with a constant inclination angle. Our analysis will focus on the last deviated well section with 65° inclination angle.

The entire process comprises several steps, as outlined below:

1) Near-field stresses σ^{I} is computed by $\sigma^{\mathrm{I}} = -S^{\mathrm{ML}} - \sigma^{\mathrm{II}} - \sigma^{\mathrm{III}}$.
2) The near-field stresses in cylindrical coordinate system, $\sigma^{\mathrm{I}}_{\theta\theta}$ and σ^{I}_{rr}, are then translated to far-field stresses using correlation:

$$\sigma_{\theta\theta}^{\mathrm{I}}=\left(1+\frac{r_w^2}{r^2}\right)P_0-\left(1+3\frac{r_w^4}{r^4}\right)S_0\cos2\theta$$

$$\sigma_{rr}^{\mathrm{I}}=\left(1-\frac{r_w^2}{r^2}\right)P_0+\left(1-4\frac{r_w^2}{r^2}+3\frac{r_w^4}{r^4}\right)S_0\cos2\theta \qquad (2)$$

$$\sigma_{zz}^{\mathrm{I}}=4\nu\frac{r_w^2}{r^2}S_0\cos2\theta+\sigma_{zz}^{\mathrm{I}}\left(r=\infty\right)$$

where $P_0=\frac{\sigma_{xx}^{\mathrm{I}}+\sigma_{yy}^{\mathrm{I}}}{2}$, $S_0=\frac{\sigma_{xx}^{\mathrm{I}}-\sigma_{yy}^{\mathrm{I}}}{2}$. In the near-field, the cylindrical coordinate system is used because all components of the poro-elastic and thermo-elastic stresses (σ^{II} and σ^{III}) exhibit axisymmetry due to the radial nature of pressure diffusion and heat conduction. Thus, σ_{xx}^{I}, σ_{yy}^{I}, and σ_{zz}^{I} in the local Cartesian coordinate system in far-field (Figure 2b) is computed by Eq. (2). Note that, since *y*-axis is aligned with the intermediate principal stress direction (*y*'), the in-plane shear stress, σ_{xy}, is zero (see detailed stress transformation analysis below).

3) The total stress in far-field is then calculated by $\sigma=\sigma^{\mathrm{I}}+\sigma^{\mathrm{II}}+\sigma^{\mathrm{III}}$ to account for the non-negligible thermo-poro-mechanical effect away from the borehole. Here, radius *r* for far-field is taken as 2.5 m.
4) The stresses are then transformed to the global coordinate system *x*'*y*'*z*' for a general wellbore geometry with an arbitrary inclination angle. In this work, a three-dimensional (3-D) stress transformation is adopted (Figure 2b). The normal and shear stresses on the local (inclined borehole) coordinate system *xyz* are obtain based on the stress values in the global coordinate system *x*'*y*'*z*', which is aligned with the three principal (in-situ) stresses (the minimum in-situ stress $S_{h\min}$, the intermediate in-situ stress $S_{H\max}$, and the maximum in-situ stress S_v).

   In the local coordinate system, the *z* axis is aligned with the direction of the well, while the *x* and *y* axes constitute the plane transverse to the wellbore. Taking l_i, m_i, n_i (*i*=1,2,3) as the direction cosines between the major axes in the local and global coordinates (for instance, l_1 stands for the direction cosine between *x* and *x*', and l_2 represents the direction cosine between *y* and *x*'), then the stress vector in Voigt form is transformed using

$$\begin{Bmatrix}\sigma_{xx}\\\sigma_{yy}\\\sigma_{zz}\\\sigma_{xy}\\\sigma_{yz}\\\sigma_{zx}\end{Bmatrix}=\begin{bmatrix}l_1^2 & m_1^2 & n_1^2 & 2l_1m_1 & 2m_1n_1 & 2l_1n_1\\ l_2^2 & m_2^2 & n_2^2 & 2l_2m_2 & 2m_2n_2 & 2l_2n_2\\ l_3^2 & m_3^2 & n_3^2 & 2l_3n_3 & 2m_3n_3 & 2l_3n_3\\ l_1l_2 & m_1m_2 & n_1n_2 & l_1m_2+l_2m_1 & m_1n_2+m_2n_1 & l_1n_2+l_2n_1\\ l_2l_3 & m_2m_3 & n_2n_3 & l_2m_3+l_3m_2 & m_2n_3+m_3n_2 & l_2n_3+l_3n_2\\ l_1l_3 & m_1m_3 & n_1n_3 & l_1m_3+l_3m_1 & m_1n_3+m_3n_1 & l_1n_3+l_3n_1\end{bmatrix}\begin{Bmatrix}-S_{h\min}\\-S_{H\max}\\-S_v\\0\\0\\0\end{Bmatrix} \qquad (3a)$$

At FORGE, both inclined well intervals of 16A(78)-32 and 16B(78)-32 are drilled on the plane parallel to the minimum in-situ stress ($S_{h\min}$) direction (i.e., *y* axis is identical to *y*' axis and is orthogonal to both *x*' and *z*' axes). We have $l_2=\cos(y,x')=0$, $n_2=\cos(y,z')=0$, $m_1=\cos(x,y')=0$, $m_2=\cos(y,y')=1$, $m_3=\cos(z,y')=0$. Consequently, σ_{xy} and σ_{yz} in Eq. (3a) are both zero. Substituting the 65° inclination angle of the inclined well relative to the vertical *z*' axis on *xz*-plane into Eq. (3a) leads to

$$\begin{Bmatrix}\sigma_{xx}\\\sigma_{yy}\\\sigma_{zz}\\\sigma_{zx}\end{Bmatrix}=\begin{bmatrix}\cos^2 65^\circ & 0 & \cos^2 25^\circ & 2\cos 65^\circ\cos 25^\circ\\ 0 & 1 & 0 & 0\\ \cos^2 155^\circ & 0 & \cos^2 65^\circ & 2\cos 155^\circ\cos 65^\circ\\ \cos 65^\circ\cos 155^\circ & 0 & \cos 25^\circ\cos 65^\circ & \cos^2 65^\circ-\cos^2 25^\circ\end{bmatrix}\begin{Bmatrix}-S_{h\min}\\-S_{H\max}\\-S_v\\0\end{Bmatrix} \qquad (3b)$$

The key question then becomes identifying the specific value of θ at a fixed distance to well ($r=4r_w$)

where P- and fast and slow S-waves correspond (i.e., the location that exhibits the greatest stress-induced wave speed anisotropy). All three stresses, $\sigma_{\theta\theta}^{\mathrm{I}}$, σ_{rr}^{I}, and σ_{zz}^{I}, exhibit monotonic trends (tension positive), either increasing or decreasing with θ. Thus, the most pronounced stress-induced wave speed anisotropy occurs at the extreme stress values, which are recovered at either $\theta = 0$ or $\theta = \frac{\pi}{2}$. Further investigation into stress magnitudes reveals the following relationships (tension positive) - when $\sigma_{xx} < \sigma_{yy}$ (for scenarios of horizontal wells or well sections with large inclination angles such as the 65° section):

$$S_3 = -\sigma_{zz}\left(r = 4r_w, \theta = \frac{\pi}{2}\right), S_2 = -\sigma_{rr}\left(r = 4r_w, \theta = \frac{\pi}{2}\right), S_1 = -\sigma_{\theta\theta}\left(r = 4r_w, \theta = \frac{\pi}{2}\right).$$

Hence, ML predicted near-field stresses under the influences of stress concentration and axisymmetric pore pressure diffusion and heat transfer are imposed at these locations to solve for all far-field stress components.

4. Result

We first solve for the far-field stresses at the depths corresponding to the core sample locations in well 16B (78)-32. Next, the ML-predicted stresses are translated into far-field stresses. Stress profiles for all three principal stress components are then generated. All input parameters are listed in Table 2. Although the geophysical and mechanical properties of rocks typically vary with depth, due to the limited availability of site-specific data for FORGE rocks, representative values for granitic rocks are assumed and applied uniformly along the entire depth interval.

Table 2: Input parameters.

Young's modulus (E)	37.5 GPa
Poisson's ratio (ν)	0.25
Density (ρ)	2710 kg/m^3
Thermal conductivity (k_T)	2.5 $\mathrm{W/(m \cdot K)}$
Volumetric thermal expansion coefficient (β_d)	8×10^{-6} K^{-1}
Thermo-elastic stress coefficient (η_d)	2×10^5 $\mathrm{N/(m^2 \cdot K)}$
Poro-elastic stress coefficient (η)	0.08
Biot effective stress coefficient (α)	0.24
Temperature difference gradient (ΔT per km) (linear reservoir temperature gradient 70 ˚C/km (Jones et al., 2024); linear pre-cooling wellbore temperature gradient 45 ˚C/km)	-25 ˚C/km
Pre-cooling duration (t_c)	10 hours
Warmup duration (t_w)	4 hours
Wellbore pressure gradient (Δp_w per km) (mud weight 9.5 ppg)	11.18 MPa/km
Reservoir pressure (p_0)	0 MPa
Wellbore radius (r_w)	0.12 m

4.1. In-situ stress estimates at core sample depths

The ML-predicted stresses (both magnitudes and the corresponding stress gradients) for the gneiss sample (Core i) are translated to far-field values using the methodology outlined in Section 3.3 under both pre-cooling and warmup scenarios (Figure 4). Both cases show that the translated minimum ($S_{h\min}$) stress in far-field is lower than the ML predictions, while the maximum (S_v) stress remains relatively unchanged, resulting in a larger stress difference between the maximum and minimum stresses. This discrepancy arises because the ML model estimates stress components oriented along the wellbore axis, which is inclined relative to the true global principal stresses.

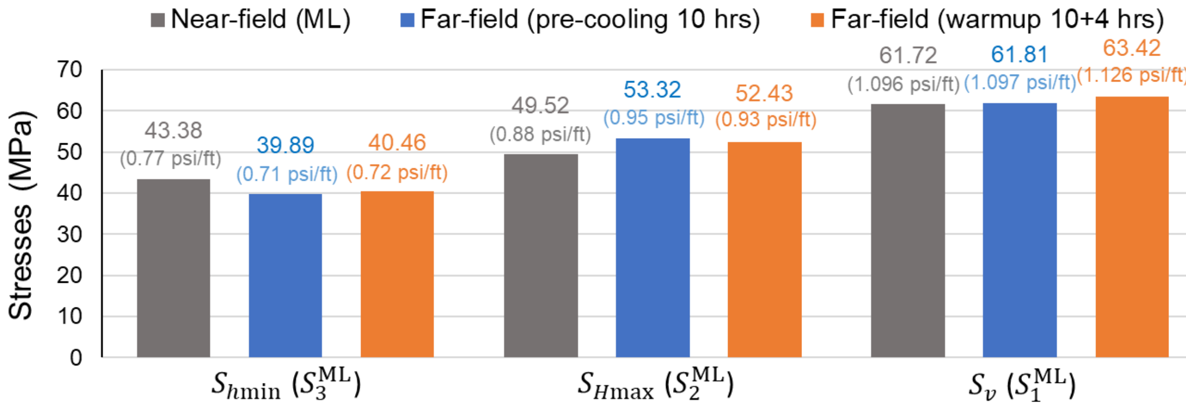

Figure 4: Near-field ML predictions and translated far-field stresses at depth of core i.

Following the same method, the far-field stresses at all core depths are computed (Table 3). All five cores are recovered from the same inclined section. Generally, pre-cooling conditions lead to smaller $S_{h\min}$ and S_v, and a larger $S_{h\max}$ compared to the warmup case. This trend is attributed to the pre-cooling induced tensile thermal stresses, which peak immediately after pre-cooling ends and then gradually dissipate over time as they propagate away from borehole.

Table 3: ML predicted near-field stresses and corresponding far-field stresses (magnitudes and converted stress gradients) at all core locations.

Rock Type	Core ID	S_1^{ML} - S_2^{ML} - S_3^{ML} (MPa & psi/ft)	TVD (m)	$S_{h\min}$ (MPa & psi/ft)		$S_{h\max}$ (MPa & psi/ft)		S_v (MPa & psi/ft)	
				Pre-cooling	Warmup	Pre-cooling	Warmup	Pre-cooling	Warmup
Gneiss	i	61.72 - 49.52 - 43.38 (1.096 – 0.88 – 0.77)	2,490	39.89 (0.71)	40.46 (0.72)	53.32 (0.95)	52.43 (0.93)	61.81 (1.097)	63.42 (1.126)
Granite	ii	60.51 - 48.94 - 44.51 (1.085 – 0.88 – 0.8)	2,466	41.67 (0.75)	42.23 (0.76)	52.75 (0.95)	51.86 (0.93)	60.03 (1.076)	61.62 (1.105)
Grano-diorite	iii	60.84 - 49.21 - 44.31 (1.09 – 0.88 – 0.79)	2,467	41.33 (0.74)	41.89 (0.75)	53.03 (0.95)	52.15 (0.93)	60.48 (1.084)	62.07 (1.112)
Quartz Gneiss	iv	60.32 - 49.58 - 42.32 (1.104 – 0.91 – 0.77)	2,416	38.95 (0.71)	39.5 (0.72)	53.5 (0.98)	52.63 (0.96)	60.38 (1.105)	61.94 (1.134)
Quartz Gneiss	v	60.64 - 49.64 - 43.40 (1.11 – 0.91 – 0.79)	2,416	40.24 (0.74)	40.78 (0.75)	53.54 (0.98)	52.67 (0.96)	60.48 (1.107)	62.03 (1.135)

4.2. Far-field stress profiles

The far-field stress profiles are plotted in Figure 5. Their values are compared with the ML predictions for all three stress components. Additional stress predictions by an elastic geomechanical model for S_v (May & Jones, 2023) is also included in Figure 5c. Observations indicate that the variation from near-field to far-field vertical stresses is the least among all three stress components, leading to good agreements across all scenarios. In contrast, $S_{h\min}$ decreases and $S_{h\max}$ increases when translated to far-field, resulting in a more anisotropic horizontal stress state compared to near-field predictions. Stress gradients are also presented in Figure 5. In both the pre-cooling and warmup scenarios, $S_{h\min}$ exhibits a stress gradient of ~0.74 psi/ft, $S_{h\max}$ has a gradient of ~0.98 psi/ft, and S_v evolves around 1.1 psi/ft.

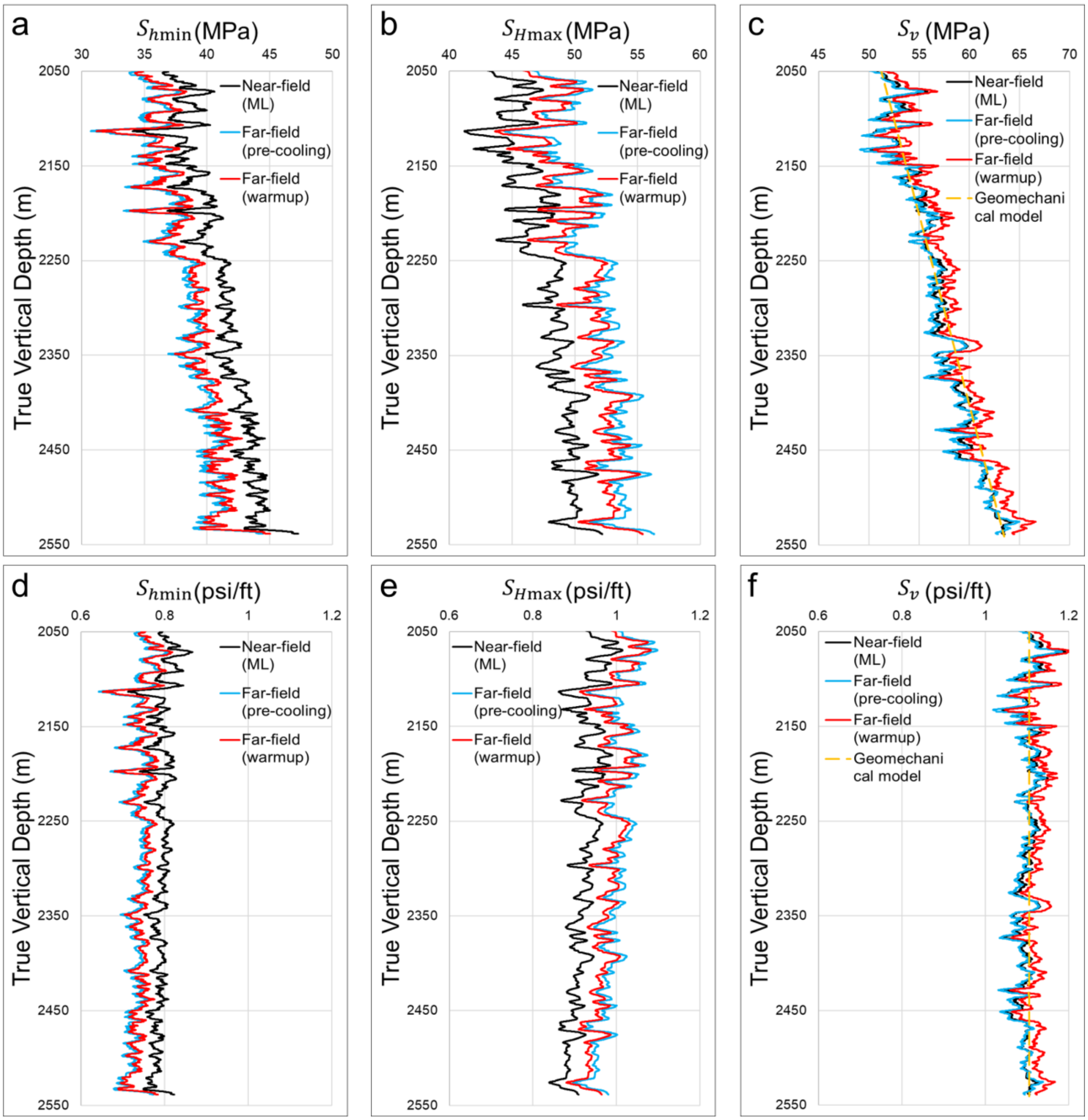

Figure 5: Stress profiles along the inclined interval of all three principal far-field stresses ($S_{h\min}$, $S_{h\max}$, S_v). The values are compared with ML-predicted near-field stresses, and geomechanical model predictions in case of vertical stress S_v.

5. Conclusions

This report presents the integrated workflow developed for estimating far-field stresses at an EGS well. The project's overall objective - to characterize in-situ stresses at Utah FORGE - was achieved by establishing a reliable velocity-to-stress model that combines laboratory TUV experiments, machine learning, and physics-based methods. Field sonic logging data were successfully incorporated to generate stress profiles along the inclined interval of well 16B(78)-32 under relevant in-situ scenarios.

6. References

Cheng, A. H. D. (2016). Poroelasticity. Springer.

Jones, C., Simmons, S., & Moore, J. (2024). Geology of the Utah frontier observatory for research in geothermal energy (FORGE) enhanced geothermal system (EGS) site. Geothermics, 122, 103054.

Lu, G., Kelley, M., Raziperchikolaee, S., & Bunger, A. P. (2024a). Modeling the impact of thermal stresses induced by wellbore cooldown on the breakdown pressure and geometry of a hydraulic fracture from an EGS well. Rock Mechanics and Rock Engineering.

Lu, G., Lu, Y., Kelley, M., Raziperchikolaee, S., & Bunger, A. P. (2024b). Thermo-poro-elastic stress alteration around an EGS well due to cold fluid circulation. In 58th US Rock Mechanics/Geomechanics Symposium, Golden, Colorado, 23–26 June 2024. ARMA-24-689.

Lu, G., Mustafa, A., & Bunger, A. (2024c). Utah FORGE 2-2439v2: Report on Predicting Far-Field Stresses Using Finite Element Modeling and Near-Wellbore Machine Learning for Well 16A(78)-32. Geothermal Data Repository. University of Pittsburgh. https://gdr.openei.org/submissions/1641

Lu, G., Mustafa, A., & Bunger, A. P. (2025). Characterizing In-Situ Stresses at Utah FORGE Using a Multi-Component Approach Combining Laboratory Experiments, Field Measurements, Physics-Based Modeling, and Machine Learning Methods. In 50th Workshop on Geothermal Reservoir Engineering, Stanford University, Stanford, California, February 10-12, 2025.

May, D., & Jones, D. (2023). Utah FORGE: Well 16B(78)-32 Logs from Schlumberger Technologies. [Dataset]. Geothermal Data Repository. Energy and Geoscience Institute at the University of Utah. https://doi.org/10.15121/2001059

Mustafa, A., Kelley, M., Lu, G., & Bunger, A. (2024). An integrated machine learning workflow to estimate in situ stresses based on downhole sonic logs and laboratory triaxial ultrasonic velocity Data. Journal of Geophysical Research - Machine Learning and Computation. 1(4), e2024JH000318.

Mustafa, A., Lu, G., & Bunger, A. (2025). Utah FORGE 2-2439v2: Estimate stress for future well 16B(78)-32 based on sonic logging data and laboratory data, enabled by the validated ML algorithm.

Xing, P., Wray, A., Velez-Arteaga, E.I., Finnila, A., Moore, J., Jones, C., Borchardt, E., & McLennan, J. (2022). In-situ stresses and fractures inferred from image logs at Utah FORGE. Proceedings: 47th Workshop on Geothermal Reservoir Engineering, Stanford University, Stanford, CA (February 2022). SGP-TR-223.